

Tuning CO₂ electroreduction by facet-dependent metal-support interaction



Jinmeng Li, Zhixiang Cheng, Junpeng Zhu, Hanxia Chen, Xiaoxue Xu, Yuheng Wang,
Juzhe Liu*, Zhongfei Xu*, Lidong Wang*

MOE Key Laboratory of Resources and Environmental Systems Optimization, College of Environmental Science and Engineering, North China Electric Power University, Beijing 102206, P.R. China

ARTICLE INFO

Keywords:

CO₂RR
Metal-Support Interaction
Facet
Electron transfer
Stability

ABSTRACT

Electrochemical carbon dioxide reduction reaction (CO₂RR) helps to build a sustainable carbon cycle system. The selectivity and stability of CO₂RR catalysts can be tuned by manipulating Metal-Support Interaction (MSI). Here, we conducted a theoretical and experimental research on the interaction between Ag nanoparticles and diverse crystal faces of Cu₂O. It was found the strong electron transfer from Ag to (100) facet of hexahedral Cu₂O enabled the formation of charge-redistributed interface with positively charged Ag and negatively charged Cu₂O, which was more favorable to the stability of integrated structure and CO₂-to-CO catalytic process compared to Ag-decorated octahedral and dodecahedral Cu₂O with exposed (111) and (110) facets, respectively. Consequently, the composite of Ag on hexahedral Cu₂O exhibited an impressive CO Faradaic efficiency of 93%, surpassing Ag on octahedral and dodecahedral Cu₂O as well as individual Ag and Cu₂O nanoparticles. This work provides an effective avenue to tune CO₂RR process by interface engineering.

1. Introduction

Electrocatalytic carbon dioxide reduction reaction (CO₂RR) into value-added chemicals and fuels holds promise in reducing the usage of fossil resources and promoting carbon neutrality [1,2]. However, improving the reaction activity and product selectivity of CO₂RR in practical applications pose a significant challenge due to its complex multiple charge-proton-transfer processes and concurrent competitive hydrogen evolution reaction (HER) [3–5]. Considerable efforts have been devoted to ameliorate CO₂RR sluggish kinetics and tailor product distribution by designing and developing electrocatalysts. Compositing metal-based nanomaterials with appropriate supporters can create featured interface with strong metal-support interaction (MSI) that may tune the electrocatalytic steps and products [6,7]. MSI can induce charge transfer and component interaction between metal and supporter which can not only stabilize metal species but also tailor the local electronic structure and coordination environment, thereby enhancing CO₂RR performance [8–10]. For instance, MSI was able to endow Au-CeO₂ with abundant Au^{δ+} species and oxygen vacancies which was in favor of CO₂ activation and formation of the key intermediate of *COOH [11]. The Cu/nanodiamond interface strengthens CO binding and promotes the production of multi-carbon products (C₂₊) by reducing the apparent barrier for CO dimerization [12]. Therefore,

deliberate manipulation on MSI through precisely constructing catalysts should provide substantial possibilities to solve the issues in CO₂RR.

MSI strongly depends on the state of supporters. As to one certain supporter, different exposed facets are associated with different atomic stacking forms and electronic structure which may affect interface structure and state of loaded metal species as well as catalytic property [7,13]. Previous studies have shown that the (100) planes of TiO₂ in Au/TiO₂ influenced the activation of O₂ and the formation and desorption of carbonates for CO oxidation [14]. Pt nanoparticles (NPs) loaded on TiO₂ (001) facet could more efficiently improve the photo-induced carrier separation efficiency than that on TiO₂ (010) facet in photoreduction of CO₂ to CH₄ [15]. Additionally, it was observed that the exposed (111) facet of CeO₂ nano-polyhedra could modulate the chemical state of loaded Cu NPs, leading to superior catalytic performance in aldehydes hydrogenation, when compared to the (110) and (100) crystal planes [16]. Although the interaction between metal and exposed facets of supporters in catalysis processes have been noticed, the corresponding research in the field of CO₂RR is in its infancy. Ag-based materials are commonly used in CO₂RR but still suffering the drawback of poor efficiency, low selectivity and high cost [17]. For enhanced performance and potential application, it is reasonable and of importance to employ a competent support to modulate their spatial locations and electron structures [18]. For that matter, Cu₂O should be

* Corresponding authors.

E-mail addresses: liujuzhe@ncepu.edu.cn (J. Liu), xuzhongfei@ncepu.edu.cn (Z. Xu), wld@ncepu.edu.cn (L. Wang).

an appropriate supporter due to its low cost, favorable electron transport property and mature synthetic method that allows precise control of exposed facet [19]. Noteworthily, different exposed facets of Cu₂O exhibit specific atom arrangement, distinctive electronic structure and surface energy, which show great potential to tune the property and electrocatalytic ability of adjacent Ag species by MSI [20–22].

In this work, we adopted silver-modified cuprous oxides (Ag/Cu₂O) as prototypes to investigate the Cu₂O facet-dependent MSI and corresponding influence on CO₂RR processes by first-principles calculations and systematic experiments. Specifically, Ag NPs were loaded on hexahedral, octahedral and dodecahedral Cu₂O (h-Cu₂O, o-Cu₂O and d-Cu₂O) with exposed facets of (100), (111), and (110), marked as Ag/h-Cu₂O, Ag/o-Cu₂O, and Ag/d-Cu₂O, respectively, which demonstrated different electron transfer properties and electrocatalytic performance. Among them, Ag/h-Cu₂O exhibited the strongest electronic interaction and displayed the most remarkable CO selectivity, as well as satisfactory structural stability. This work can offer an effective strategy to control the CO₂RR performance of metal-supporter composites.

2. Experimental procedures

2.1. Materials synthesis

2.1.1. Synthesis of Cu₂O

Typically, h-Cu₂O particles were synthesized as follows [22,23]. NaOH aqueous solution (2 M; 10 mL) was dropped into CuCl₂·2 H₂O aqueous solution (0.01 M; 100 mL) through a pipette. After stirring for 0.5 h, ascorbic acid (AA) solution (0.6 M; 10 mL) was added dropwise into the blue solution. The mixture was stirred for 3 h in a water bath at 10 °C and the solution gradually turned orange-yellow. The resulting precipitate was collected by centrifugation and washed with distilled water and absolute ethanol for 3 times respectively. Finally, the h-Cu₂O product was obtained after drying under vacuum at 60 °C for 8 h. o-Cu₂O was fabricated by the same method except for adding 4.5 g polyvinylpyrrolidone (PVP, MW 30 000) into CuCl₂·2 H₂O aqueous solution and changing the bath temperature to 30 °C. d-Cu₂O was synthesized by the same method of preparing h-Cu₂O except for adding mixed solution of 4.5 mL oleic acid (OA) and 20.0 mL ethanol into CuCl₂·2 H₂O aqueous solution and controlling the bath temperature at 55 °C.

2.1.2. Synthesis of Ag/Cu₂O

For fabricating Ag/h-Cu₂O, 10 mg h-Cu₂O was dispersed in 200 mL distilled water by ultrasonic vibration for 0.5 h, then sodium citrate aqueous solution (0.03 M; 2 mL), NaBH₄ aqueous solution (0.1 M; 0.7 mL) and AgNO₃ aqueous solution (0.01 M; 0.7 mL) were dropped sequentially into the vigorously stirred solution containing Cu₂O particles. The color of the solution changed from orange to tan, indicating the formation of small Ag nanoparticles. As the reaction continued for 1 h in a water bath at 20 °C, the color of the solution gradually deepened, indicating the formation of Ag/h-Cu₂O [24]. Ag/o-Cu₂O and Ag/d-Cu₂O were synthesized by the same method. The Ag/Cu atomic ratios of Ag/h-Cu₂O, Ag/o-Cu₂O and Ag/d-Cu₂O measured by inductively coupled plasma optical emission spectroscopy (ICP-OES) are 10.3, 11.2 and 9.7%, respectively. By adjusting the feeding amount of AgNO₃, we obtained Ag/h-Cu₂O with different Ag loadings, and the Ag/Cu atomic ratio measured by ICP-OES were about 5.2%, 10.3%, 14.5% and 19.0%, respectively. The size of Ag nanoparticles could be adjusted by varying the synthesis temperature to 0, 20, 40, and 60 °C.

2.2. Materials characterizations

The phase and structure of the materials were characterized by X-Ray Diffractometer (XRD, Smart Lab SE) with Cu K α radiation ($\lambda=1.5406\text{ \AA}$, scan rate = 10° min⁻¹). Scanning electronic microscope (SEM, Zeiss Gemini 300 SEM) was employed to determine the morphology of the

materials. Transmission electronic microscope (TEM) and high-resolution TEM (HRTEM, JOEL 2100 TEM) were utilized to identify the microstructures of different materials. The X-ray photoelectron spectrometer (XPS, ESCALAB 250xi) was employed to characterize the composition of the materials. All the XPS spectra were referenced to the binding energy of the C 1 s peak at 284.8 eV. The Brunauer-Emmett-Teller (BET) method was performed to calculate the specific surface area of the materials. The Fourier transform infrared spectroscopy (FT-IR, Shimadzu IRTracer-100) was carried out to obtain the chemical bonds or functional information of different materials. The isotopic tracing test was performed on QP2020 GC/MS (Shimadz) by using ¹³CO₂ as reactants under the same as test condition of electrocatalytic CO₂ reduction.

2.3. X-ray absorption spectroscopy (XAS)

Cu K-edge X-ray absorption spectroscopy was performed at 1W2B beamline in the Beijing Synchrotron Radiation Facility (BSRF) in fluorescence mode, used a Si (111) double-crystal monochromator. Ag K-edge X-ray absorption spectroscopy was performed at BL14W1 beamline in Shanghai Synchrotron Radiation Facility (SSRF) in transmission mode, using a Si (311) double-crystal monochromator. In the testing, Cu-foil and Ag-foil were used to calibrate the energy respectively.

2.4. In situ Raman spectroscopy

Raman spectra were collected on a confocal Raman microscope (Jobin Yvon Raman spectrometer model HR800) with a 633 nm laser as an excitation source (100 ~ 3000 cm⁻¹). The electrochemical test was performed in an electrolytic cell with three-electrode configuration (EC-Raman-H). A glass carbon electrode loaded with 0.5 mg cm⁻² catalyst, an Ag/AgCl (saturated KCl solution) and a graphite rod were used as working, reference and counter electrode, respectively. Nafion117 proton exchange membrane was used to separate the catholyte and anolyte. In the Raman test, CO₂-saturated 0.1 M KHCO₃ was continuously injected into the electrolytic cell at a rate of 10 mL min⁻¹.

2.5. Electrochemical measurements

The electrocatalytic experiment was performed with an electrochemical station (CHI 760E) in a two-compartment electrochemical cell where the anodic and cathodic compartments were separated by a Nafion117 proton exchange membrane. Both anode and cathode chambers were filled with 30 mL 0.1 M KHCO₃ solution. In the cathode chamber, the carbon paper loaded with 0.5 mg cm⁻² catalyst and an Ag/AgCl (saturated KCl solution) were used as working and reference electrode, respectively. A Pt foil electrode (3×1 cm; 1 mm thick) was used as the counter electrode in the anodic chamber. Before the test of CO₂RR, CO₂ (99.999%) was continuously pumped into the cathodic electrolyte with an average flow rate of 30 mL min⁻¹ for 30 min. Linear sweep voltammetry (LSV) curves were collected (no iR-corrected) at a scan rate of 50 mV s⁻¹ after the activating treatment of performing cyclic voltammetry (CV) for 20 cycles at a rate of 20 mV s⁻¹ at 0 to -0.5 V until the change in current was negligible using electrochemical station. CO₂ reduction products were collected by chronoamperometry measurement at constant potential for 1 h.

The gaseous products (H₂, CO and other gaseous hydrocarbons) were quantified by an online gas chromatograph system (FULI GC9790PLUS) equipped with a flame ionization detector (FID) and a thermal conductivity detector (TCD). The following equation are used to calculate the Faradaic efficiencies (FEs) of gaseous products [25].

$$FE_{gaseous} \% = \frac{P_0 \times V_0 \times Z_i \times v(vol\%) \times F}{R \times T \times I \times 60(s \text{ min}^{-1})} \times 100\%$$

Here, P₀ is the standard atmospheric pressure, V₀ is the gas flow rate,

Z_i is the number of electrons transferred for the formation of certain gas products, v (vol%) is the volume ratio of gas products, R is the gas constant ($8.314 \text{ m}^3 \text{ Pa mol}^{-1} \text{ K}^{-1}$), T is 298 K, F is the Faraday constant ($96,485 \text{ C mol}^{-1}$), I is steady-state current.

The liquid products were measured by 600 M Hz ^1H nuclear magnetic resonance (NMR) spectroscopy, and a certain amount of dimethyl sulfoxide (DMSO) was added as the internal standards. The following equation are used to calculate the (FEs) of liquid products.

$$FE_{\text{liquid}}\% = \frac{Q_{\text{liquid}}}{Q_{\text{CA}}} \times 100\% = \frac{2 \times N_{\text{liquid}} \times F}{Q_{\text{CA}}} \times 100\%$$

N_{liquid} is the number of moles of liquid product, Q_{CA} is the total charge during electrolysis.

2.6. DFT calculations

All DFT calculations were performed using the Vienna Ab initio Simulation Package (VASP) based on the projector augmented wave (PAW) method. For the exchange-correlation energy, the Perdew-Burke-Ernzerhof (PBE) functional at the generalized gradient approximation (GGA) level was used. A plane-wave basis set with the cut-off kinetic energy of 400 eV was used. The k-point sampling of the Brillouin zone was set as gamma only. The convergence criteria for the electronic and structural optimization loop were set to 10^{-5} eV and $0.02 \text{ eV}/\text{\AA}$, respectively. A vacuum region of 15 \AA above slab was used to ensure the decoupling between neighboring systems.

The surface energy is a critical index of the stability of different facets, and the negative value always indicate a stable facet. All the possible facets of Cu_2O (001), (101), and (111) facets are considered, as shown in Fig. S1. Finally, we selected the most stable models for Cu_2O (001), (101), and (111) facets for the calculations in our paper. The surface energy E_{surf} is calculated as

$$E_{\text{surf}} = E_{\text{slab}} - N \cdot E_{\text{Cu2O}} - n \cdot \mu_x$$

E_{slab} is the total energy of different Cu_2O slab models with possible exposed atoms, E_{Cu2O} is the total energy of bulk Cu_2O and μ_x is the chemical potential of Cu or O atoms under different environment. N is the number of unit cell of Cu_2O contains in the slab model, while n is the number of Cu or O atoms which are less or more in the slab model.

The work function reflects the energy for an electron escaping from the surface of material to the vacuum, which could effectively criticize the ability of receiving and losing electrons. Work function ϕ can be calculated as the difference between vacuum level E_v and fermi level E_f

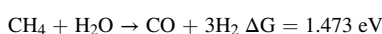
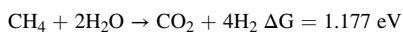
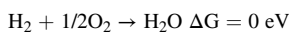
$$\phi = E_v - E_f$$

We calculated the work function for selected Cu_2O (001), (101), (111) faces, and Ag (111) facet.

The Gibbs free energies of reaction intermediates are calculated based on the computational hydrogen electrode (CHE) method, according to the equation as following

$$G = E + E_{\text{ZPE}} - TS$$

where E is the total energy of the system adsorbed with intermediates. E_{ZPE} and S is the zero-point energy and entropy of intermediates, respectively. T is the temperature, which are set as 298 K for all calculations. The values of E_{ZPE} and S can be obtained by vibration frequency calculation. All the free energies of the molecules and intermediates are calculated from H_2 , H_2O , CH_4 molecules from following reactions



3. Results and discussion

3.1. Theoretical calculation

We began by calculating the work function (E_{wf}) of Ag and (100), (110) and (111) facets of Cu_2O to indicate the possible electron transfer properties at the heterogeneous interfaces. As shown in Fig. S2, the larger work function values of Cu_2O facets than Ag suggests spontaneous electron transfer from Ag to Cu_2O facets when they are contacted. The electric potential difference between the Cu_2O (100) facet and Ag is approximately equal to that of Cu_2O (111) facet and Ag, and apparently larger than that of Cu_2O (110) facet and Ag, which implies that Ag can donate more electrons to Cu_2O (100) facet and Cu_2O (111) facet in comparison with Cu_2O (110) facet. The charge density differences of integrated systems are displayed in Fig. 1a. Stronger directional electron transfer from metal to supporter and more obvious covalent character are noticed on Ag/h- Cu_2O in comparison with Ag/o- Cu_2O and Ag/d- Cu_2O responding to more intense interaction between Ag and Cu_2O (100) facet. Furthermore, we calculated planer average charge density difference ($\Delta\rho$), which is a quantitative measure of the charge reorganization in the combined system. As shown in Fig. 1b, the black line distinguishes the interfacial position between Cu_2O facets and Ag, and the positive (negative) values of $\Delta\rho$ signify electron density accumulation (depletion) patterns [26]. Significantly, more positive and negative peaks were observed for Cu_2O and Ag of Ag/h- Cu_2O indicative of more pronounced charge reorganization with electron-rich Cu_2O and electron-deficient Ag induced by charge transfer from Ag to Cu_2O (100) facet. We also calculated the density of states (DOS) for the Ag on different Cu_2O facets along with the pure Ag (Fig. S3). Interestingly, Ag presents nonmetallic character when loaded on the Cu_2O (100) facet, which is indicative of a strong interaction and substantial charge transfer between them. In contrast, Ag loaded on Cu_2O (111) facet shows mixing covalent and metallic characters while Ag on Cu_2O (110) only demonstrates clearly metallic character similar with pure Ag cluster. These results strongly suggest that varying degrees of interfacial interaction can be achieved by attaching Ag to different Cu_2O exposed facets in order of (100), (111), and (110) based on metal-supporter electron transfer.

To build optimized catalysts, structural stability should be an important consideration factor. The reduction of high-valence Cu species is generally existed in CO_2 RR by extracting coordinated O elements, which lead to the damage of initial structure and catalytic sites. Here, we calculated the oxygen vacancy formation energy ($E_{\text{form}}-V_0$) to evaluate the structural stability of different interfaces. In Fig. 1c, the positions of box plots suggest the stability order of the Ag/ Cu_2O interfaces is Ag/h- $\text{Cu}_2\text{O} > \text{Ag/o-Cu}_2\text{O} > \text{Ag/d-Cu}_2\text{O}$. More stable interface is beneficial for restraining catalyst reconstruction and improving catalytic selectivity.

Moreover, to unveil the role of facet-dependent MSI in CO_2 RR energetics, we calculated the adsorption behaviors of CO_2 and step-by-step Gibbs free energies (ΔG) on different Ag/ Cu_2O systems and pure Ag (Fig. 1d). The adsorption and activation of CO_2 is of great importance for the electrochemical CO_2 reduction reaction. Notably, the negative ΔG values of CO_2 adsorption step for Ag/h- Cu_2O and Ag/o- Cu_2O composites indicate that these processes are exothermic and spontaneous. In contrast, Ag system exhibits positive ΔG of 0.61 eV for CO_2 adsorption which is the rate limiting step. Especially, CO_2 molecule can be bent at the interface of Ag/h- Cu_2O while it represents a linear structure on Ag, suggesting that CO_2 molecule is easily activated at the charge-redistributed heterogeneous interface (Fig. S4). The rate limiting step for Ag/h- Cu_2O and Ag/o- Cu_2O is CO desorption and corresponding ΔG values are calculated to be 0.33 eV and 0.66 eV, respectively. The conversion of COOH^* -to- CO^* is the rate limiting step of Ag/d- Cu_2O and relevant ΔG is 1.0 eV. Accordingly, the occurrence of CO_2 -to-CO conversion is more favorable on Ag/h- Cu_2O in energetics due to its lowest

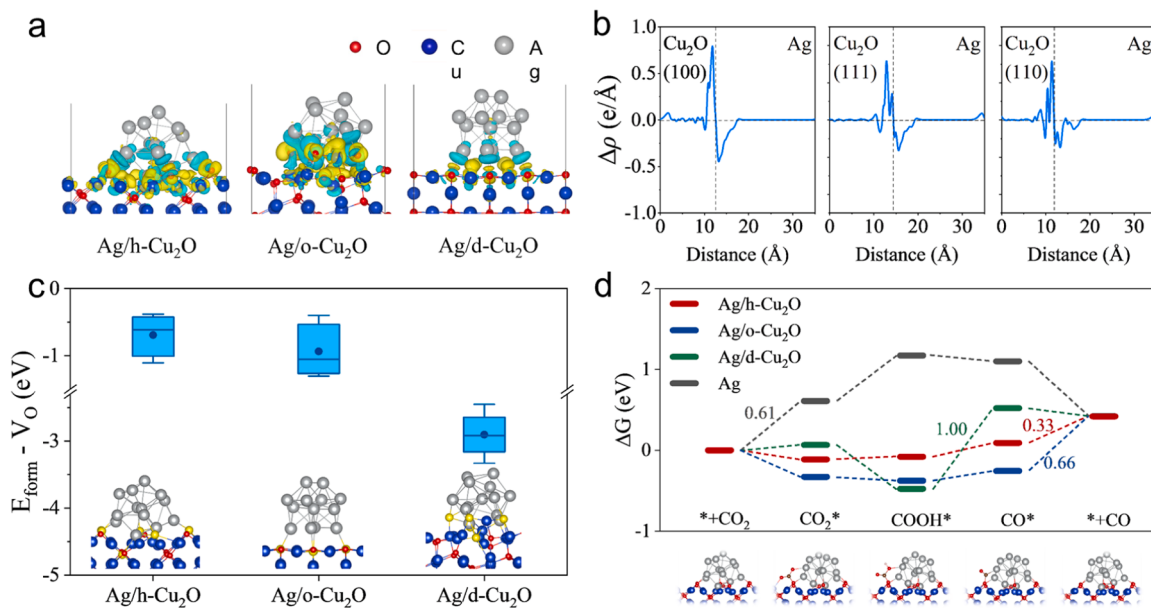


Fig. 1. (a) The charge density difference of Ag/h-Cu₂O, Ag/o-Cu₂O, and Ag/d-Cu₂O. Yellow and blue areas represent accepting and donating electrons. (b) The $\Delta\rho$ diagram of three composites. (c) The $E_{\text{form}} - V_o$ box plots at interfaces for three models, and all the possible oxygen vacancies at different interfaces are considered which are indicated as yellow balls. (d) Gibbs free energy landscape of three composites and Ag for CO₂RR route to form CO. The corresponding adsorption configurations of Ag/h-Cu₂O are also shown.

ΔG of the rate limiting step, which correspond to a lower theoretical onset potential.

Thus, facet-dependent MSI of Ag/Cu₂O catalyst systems was investigated by theoretical calculation, indicating that attaching Ag on Cu₂O (100) facet could afford modulated electron structure, relatively stable geometric structure and optimized catalytic energetics for CO₂RR to CO.

3.2. Characterization and structure analysis of Ag/Cu₂O

Inspired by the results obtained from DFT simulations, we undertook the preparation of various forms of Cu₂O decorated with Ag. Initially, the ascorbic acid reduction method was employed to prepare h-, o- and d-Cu₂O NPs with different exposed facets [27,28]. As shown in Fig. S5-S8, h-Cu₂O in cubic shape with a particle size of approximately 200 nm was fabricated when none surfactant was added. In comparison, o- and d-Cu₂O nanoparticles in similar sizes were obtained by using PVP and OA as surfactants, which demonstrated typical octahedral and dodecahedral morphology, respectively. The lattice fringes in the HRTEM images (Fig. S9-S11) further verify that the h-, o-, and d-Cu₂O are enclosed by (100) facets, (111) facets and (110) facets, respectively [20,29]. The X-ray diffraction (XRD) pattern shows six different characteristic peaks at 29.6, 36.5, 42.4, 61.5, 73.7, and 77.6 °corresponding to the characteristic (110), (111), (200), (220), (311) and (222) faces of Cu₂O (JCPDS No.05-0667) (Fig. S12) [30]. FT-IR results excluded the existence of residual capping ligands on three Cu₂O materials (Fig. S13). Afterwards, we utilized the sodium borohydride reduction method to deposit Ag NPs onto different Cu₂O surfaces [31]. SEM images in Fig. S14-S16 shows that the as-prepared Ag/Cu₂O inherited the profiles of Cu₂O but exhibits uneven morphologies and the characteristics of deposited Ag NPs. The detailed heterostructures of Ag/Cu₂O are demonstrated by TEM that Ag NPs with a diameter of 10–20 nm sporadically adorn the Cu₂O surface (Fig. 2b-d and Fig. S17). The interplanar spacing distances of 0.23 nm points towards the Ag (111) facet, and adjacent regions demonstrate typical lattice spacings of Cu₂O (100), (111) and (110) facets, which confirm the fact of Ag loading on different Cu₂O NPs (Fig. 2e-g) [20,29]. The element mapping images further confirm the presence of the Ag on the surface of the Cu₂O nanocrystals (Fig. S18-S20). The corresponding XRD pattern in Fig. S21

demonstrates the coexistence of Ag and Cu₂O.

X-ray photoelectron spectroscopy (XPS) and Auger electron spectroscopy (AES) were performed on Cu₂O and Ag/Cu₂O materials to study the electronic structures of Cu and Ag. The peaks at approximately 952.5 and 932.7 eV for different Ag/Cu₂O materials are ascribed to Cu 2p_{5/2} and 2p_{3/2}, respectively (Fig. 3a). The oxidation states of Cu in three Ag/Cu₂O materials are confirmed to be +1 by the characteristic peaks at 916.7 eV in Cu LMM AES (Fig. S22). The Ag 3d spectra of Ag NPs and Ag/Cu₂O exhibit two primary doublet peaks at ~368.2 eV and ~374.3 eV, confirming their metallic states (Fig. 3b). Notably, the Cu 2p and Ag 3d peaks of Ag/h-Cu₂O and Ag/o-Cu₂O shift to lower and higher binding energy, respectively, in comparison with Ag/d-Cu₂O and pure hexahedral Cu₂O. This suggested that the heterojunction Ag/h-Cu₂O and Ag/o-Cu₂O had strong electronic interaction and the electron transferred from the Ag to the Cu₂O via the interface [32,33]. Stronger interfacial interaction should exist in Ag and Cu₂O (100) facet for the more distinct peak shift, which is consistent with DFT results.

X-ray absorption spectroscopy (XAS) was further applied to determine the local coordination environment and electronic structure of the catalysts. In Fig. 3c, the Cu absorption edges of Ag/h-Cu₂O, Ag/o-Cu₂O and Ag/d-Cu₂O are closed to that of reference h-Cu₂O in X-ray absorption near-edge structure (XANES) spectra. In addition, extended X-ray absorption fine structure (EXAFS) spectra of three Ag/Cu₂O catalysts shows two characteristic peaks at 1.5 and 2.7 Å, which are coincident with those of Cu₂O (Fig. 3d). These results demonstrated that the structure of Cu₂O nanocrystals remains intact after decorating with Ag. Notably, the absorption edge position of Ag/h-Cu₂O demonstrates a slight downshift to lower energy compared with Cu₂O, which should be attributed to decreased oxidation state of Cu caused by strong electron transfer [34]. As shown in Fig. 3e and f, the Ag/Cu₂O composites exhibit similar Ag K-edge XANES and EXAFS spectra to pure Ag NPs and Ag foil. However, it should be noted that the Ag K-edge XANES spectra of Ag/h-Cu₂O, Ag/o-Cu₂O and Ag/d-Cu₂O gradually shift toward lower energies, which should be attributed to gradual weakening of charge transfer [35,36].

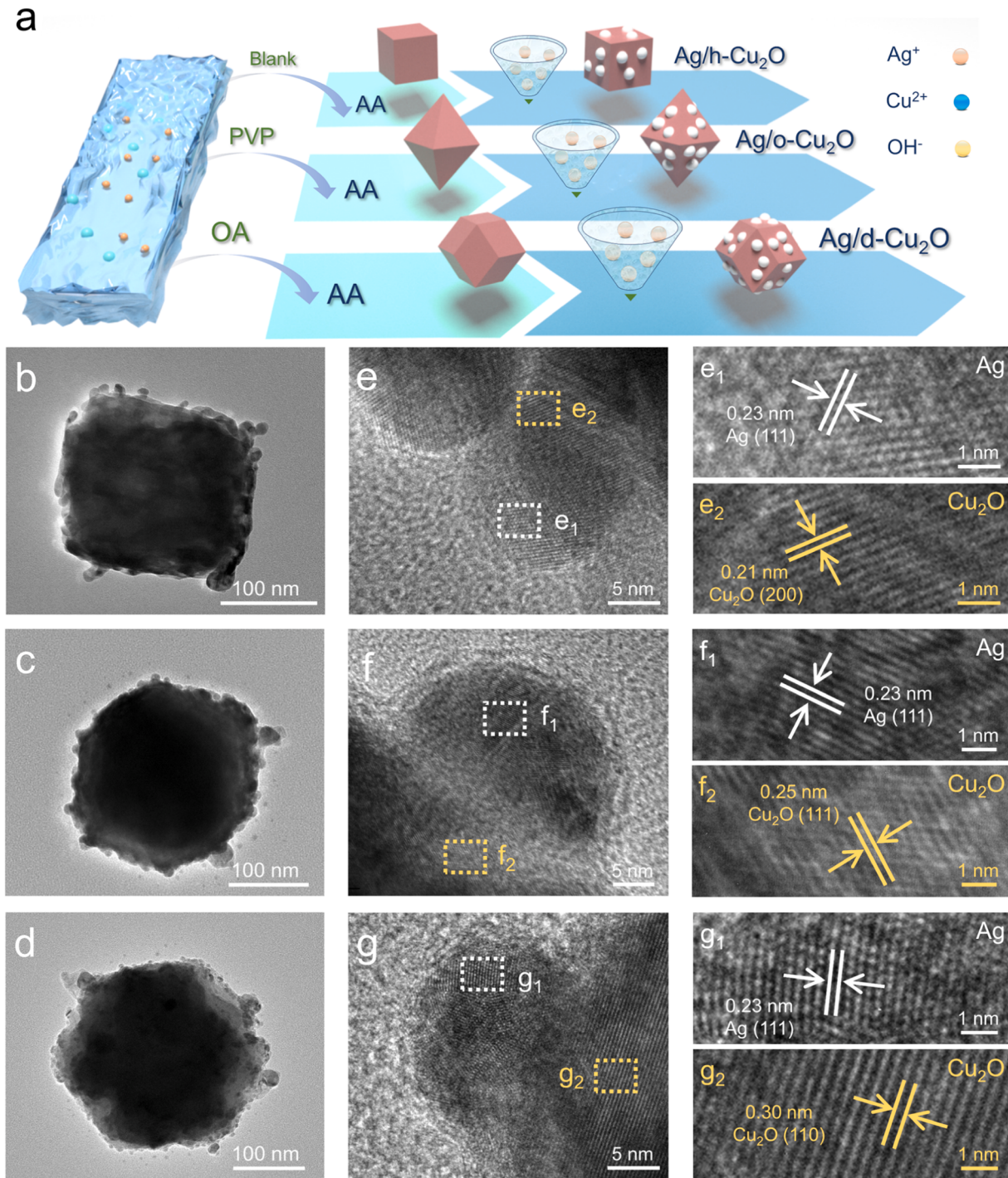


Fig. 2. (a) Synthesis schematic diagram for different catalytic materials. (b-d) TEM images and (e-g) HRTEM images of Ag/h-Cu₂O, Ag/o-Cu₂O and Ag/d-Cu₂O, respectively.

3.3. Facet-dependent CO₂RR performance of Ag/Cu₂O

The electrochemical performance tests were carried out using a three-electrode electrochemical system in a Nafion 117 proton exchange membrane separated H-cell. Preliminarily, the CO₂RR activity of our catalyst was confirmed by performing LSV on Ag/h-Cu₂O in 0.1 M KHCO₃ aqueous solutions saturated with Ar and CO₂ (Fig. S23). Optimal Ag grain size and atomic ratio of Ag/Cu were determined to be 10–20 nm and ~10% for Ag/h-Cu₂O (Fig. S24–S26). Subsequently, a series of materials were employed to investigate the influence of facet-dependent metal support interactions on CO₂RR. According to the LSV

curves after the activation process, Ag/h-Cu₂O exhibited the lowest onset potential around –0.3 V vs. RHE and the highest current density, indicating its superior CO₂RR kinetics. Meanwhile, Ag/h-Cu₂O showed a broad potential of CO selectivity that CO Faradic efficiency (FE_{CO}) exceeded 80% in the range from –0.76 V to –1.06 V and reached the top about 93% at –0.96 V with a remarkable current density of 6.5 mA·cm^{–2} (Fig. 4a). In Fig. 4b and Fig. S27, the FEs of products for different catalysts are presented. All the Cu₂O materials exhibited inferior catalytic selectivity with a high-proportioned H₂ and several carbonic products including CO, HCOOH and CH₃CH₂OH, which could be ameliorated by decorating Ag onto their surfaces. Importantly, FE_{H2}

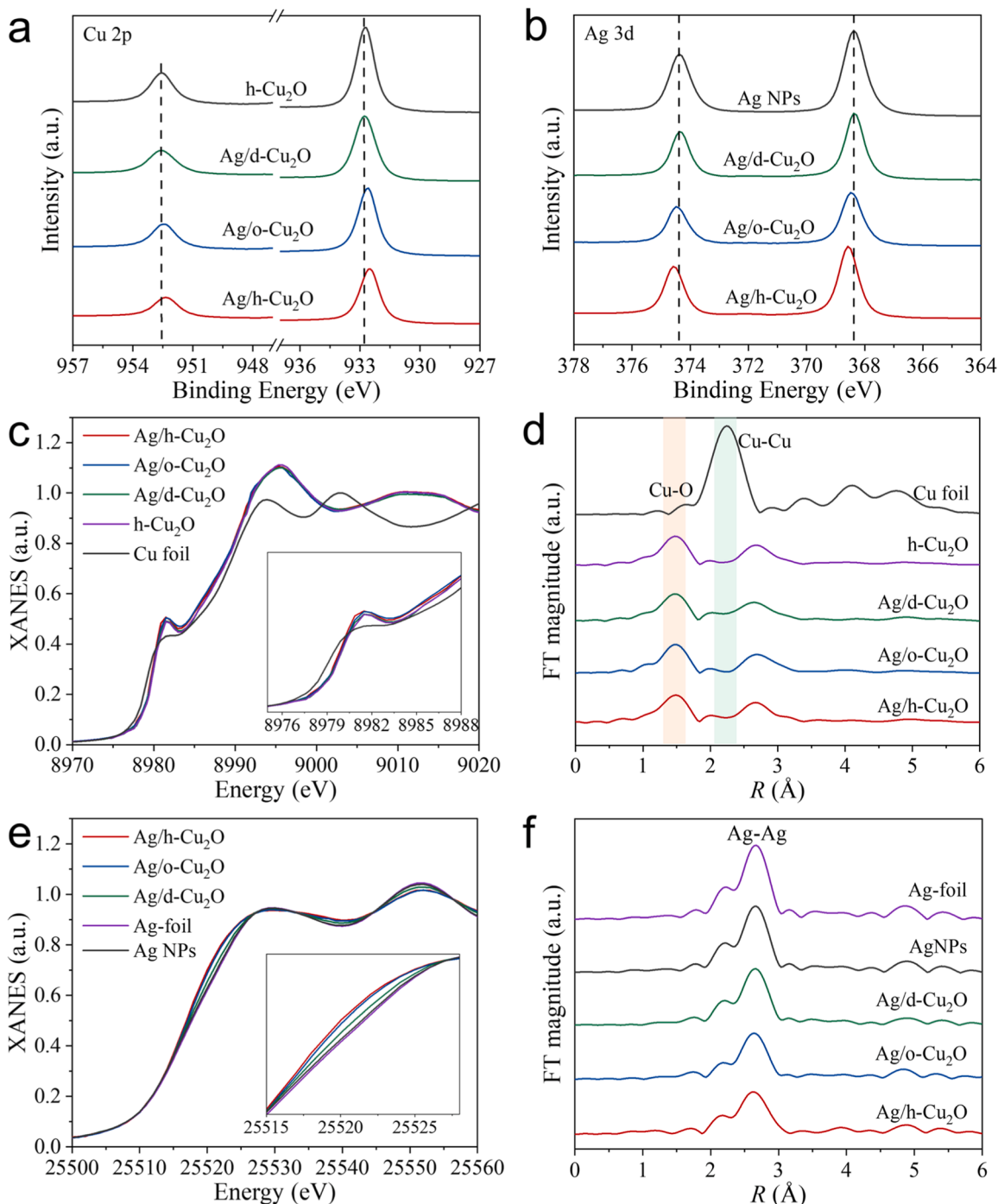


Fig. 3. Spectroscopic characterizations of different Ag/Cu₂O materials and counterparts. (a) Cu 2p and (b) Ag 3d XPS spectra. Cu K-edge (c) XANES and (d) EXAFS spectra. Ag K-edge (e) XANES and (f) EXAFS spectra.

decreased and FE_{CO} increased in the order of Ag/d-Cu₂O, Ag/o-Cu₂O and Ag/h-Cu₂O, suggesting HER was suppressed and CO₂-to-CO reaction was promoted as the interfacial interaction became stronger. As a result, Ag/h-Cu₂O displayed optimized selectivity to CO which is even higher than that of Ag NPs (69%) and in the front rank of the same kind materials (Table S1). Here, the influence of difference in specific surface areas of different materials on CO₂RR performance can be excluded by BET analysis (Fig. S28). In addition, the isotopic labeling experiment over Ag/h-Cu₂O catalyst was performed to verify the CO₂ as the only carbon source for carbon-containing products (Fig. S29).

Electrochemical active surface areas (ECSAs) of different materials were evaluated based on double layer capacitances of electrode, which

can be represented by the linear slopes of the charging current density differences plotted against scan rates (Fig. 4c and Fig. S30). Apparently, Ag/h-Cu₂O has a linear slope value (1.21 mF cm⁻²) higher than those of Ag/o-Cu₂O (0.97 mF cm⁻²) and Ag/d-Cu₂O (0.98 mF cm⁻²), and nearly 3-times higher than that of h-Cu₂O (0.32 mF cm⁻²). This strongly implies that Ag/h-Cu₂O possesses a larger ECSA than counterparts and the decorating of Ag onto Cu₂O can create more accessible active sites [37]. Electrochemical impedance spectroscopy (EIS) was performed to investigate the charge transfer kinetics for CO₂RR. As shown in Fig. S31, Ag/h-Cu₂O shows the smallest circle radius, indicating the lowest charge-transfer resistance and superior reaction kinetics [38,39]. The catalytic stability was determined through chronoamperometric

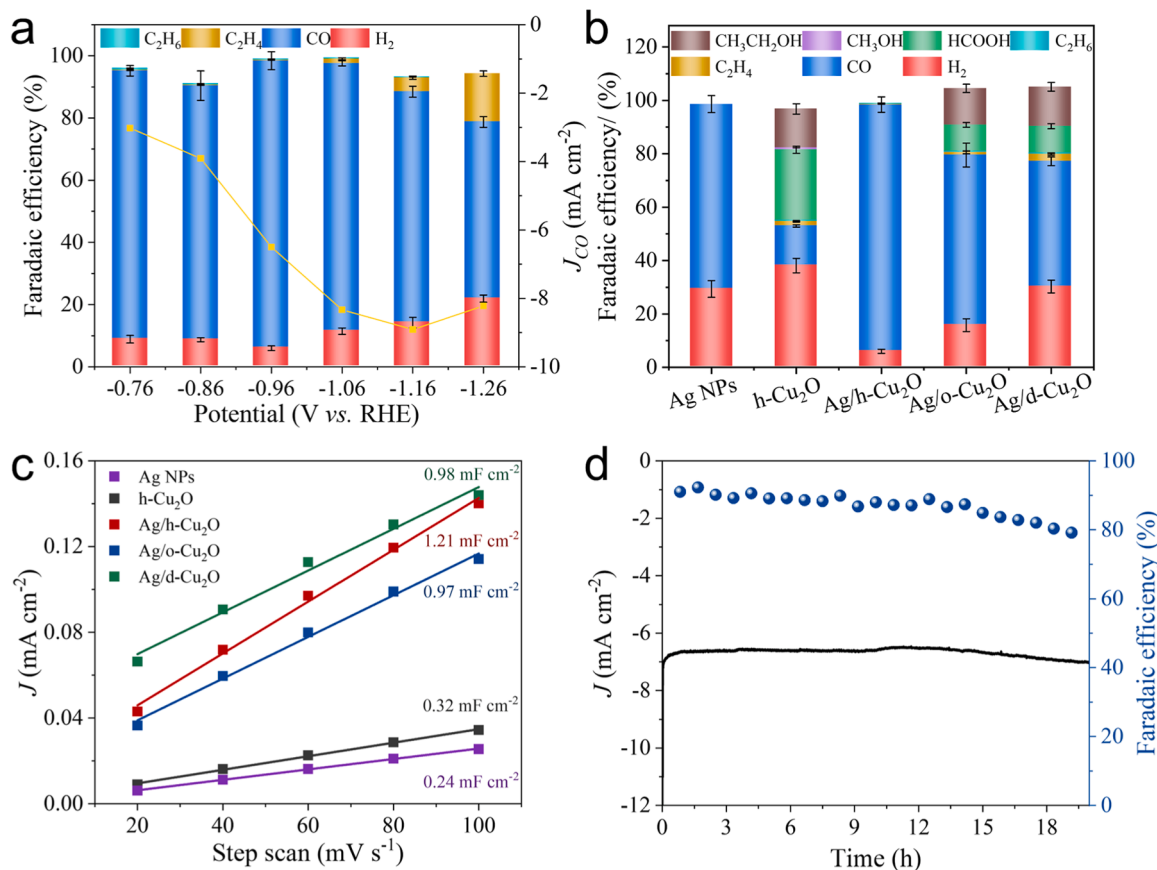


Fig. 4. (a) FEs and current densities of electrocatalytic CO₂RR products on Ag/h-Cu₂O at various potentials. (b) FEs of electrocatalytic CO₂RR products on the prepared catalysts at -0.96 V vs. RHE within 1 hour. (c) C_{dl} fitting curves of different electrocatalysts in CO₂-saturated 0.1 M KHCO₃ electrolyte. (d) Long-term stability test for Ag/h-Cu₂O electrodes.

measurements (i–t) under a constant potential of -0.96 V vs. RHE. Fig. 4d revealed that the FE_{CO} of Ag/h-Cu₂O could be maintained above at approximately 80% over 20 hours of operation without appreciable decrease on current density, demonstrating its superior stability in comparison with Ag/o-Cu₂O and Ag/d-Cu₂O (Fig. S32). The observed long-term durability could be attributed to the structural stability induced by the strong interaction between Ag and Cu₂O (100).

To realize the in-depth structure-activity relationship of CO₂RR catalysts, we investigated the structural transformation of the catalysts in electrocatalysis processes. *In situ* Raman spectroscopy were employed to directly monitor their catalytic behaviors and reactive intermediates under CO₂RR conditions (Fig. 5a). Initially, Ag/h-Cu₂O, Ag/o-Cu₂O, and Ag/d-Cu₂O exhibited two peaks at 527 and 625 cm⁻¹ corresponding to Cu₂O when the open circuit potentials were applied [40]. These characteristic peaks remained unchanged for three composites after the activation processes. Meanwhile, the peak at 356 cm⁻¹ assigned to Cu-CO stretching vibration appeared, which demonstrated the presence of adsorbed *CO on Cu [40]. Once applying the potential of -0.96 V vs. RHE, characteristic peaks of Cu₂O became ambiguous for Ag/o-Cu₂O and Ag/d-Cu₂O, while they remained for Ag/h-Cu₂O, suggesting that the structure of Ag/h-Cu₂O was relatively stable even in a reductive environment. In the meantime, three peaks at 730, 1130, and 1530 cm⁻¹ were observed and assigned to *COO⁻ [41,42], which was an important intermediate for CO₂RR. It should be noted that the COO⁻ bands of Ag/h-Cu₂O were significantly lower than those of Ag/o-Cu₂O and Ag/d-Cu₂O, indicating the rapid conversion of *COOH to *CO followed by the release of CO. To further gain insight into the changes in structure of catalytic materials during CO₂RR, *in situ* XAS technique were used. As shown in Fig. 5b, the absorption edge of Ag/h-Cu₂O in *in situ* state (Ag/h-Cu₂O-*in situ*) located at between h-Cu₂O and Cu foil, revealing

only partial reduction of h-Cu₂O supporter during CO₂RR. In contrast, after applying reduction potential, Ag/o-Cu₂O-*in situ* and Ag/d-Cu₂O-*in situ* demonstrated similar absorption edges to Cu foil, indicating a significant fraction of Cu⁺ was reduced to Cu⁰. The EXAFS data were shown in Fig. 5c to describe the coordination states of materials. It is evident that Ag/o-Cu₂O-*in situ* and Ag/d-Cu₂O-*in situ* exhibited negligible Cu-O scattering peaks at ~1.5 Å and prominent Cu-Cu bond scattering peaks at ~2.4 Å under the electrochemical condition, indicating o-Cu₂O and d-Cu₂O were mostly reduced to metallic Cu. On the other hand, Ag/h-Cu₂O-*in situ* exhibited apparent Cu-O scattering peak and a broaden peak from 1.8 to 3.3 Å which should origin from the joint contribution of Cu-Cu coordination in metallic Cu and Cu₂O at the CO₂RR potential. The curve-fitting analysis of FT-EXAFS (Figure S33 and Table S2) further showed that Ag/h-Cu₂O-*in situ* exhibited an analogous Cu-O bond distance (1.86 Å) to h-Cu₂O and a decreased Cu-O coordination number. In contrast, the Cu-Cu bond distances of Ag/d-Cu₂O-*in situ* and Ag/o-Cu₂O-*in situ* are 2.53 and 2.54 Å in line with Cu foil. These results strongly suggested that Ag/h-Cu₂O was partially reduced in *operando* electrocatalysis process consistent with Raman results. In addition, the surficial valence states of Cu sites in different catalysts after the electrocatalytic reaction were detected by AES, as shown in Fig. 5d. The surficial Cu/Cu⁺ ratios of Ag/h-Cu₂O, Ag/o-Cu₂O, and Ag/d-Cu₂O after 1 hour of CO₂RR were determined to be 0.15, 0.41, and 0.80, respectively, suggesting the superior stability of Ag/h-Cu₂O. Moreover, the Ag/h-Cu₂O exhibited surficial Cu/Cu⁺ ratios of 0.19 and 0.24 after 3 and 5 hours of electrolysis (Fig. S34), confirming its long-time structural stability, which demonstrated advantage over some catalytic materials in other reports [43–46]. The well-maintained morphology, interfacial structure and content of Cu⁺ species of Ag/h-Cu₂O after 1 hour electrocatalysis and long-time stability test also

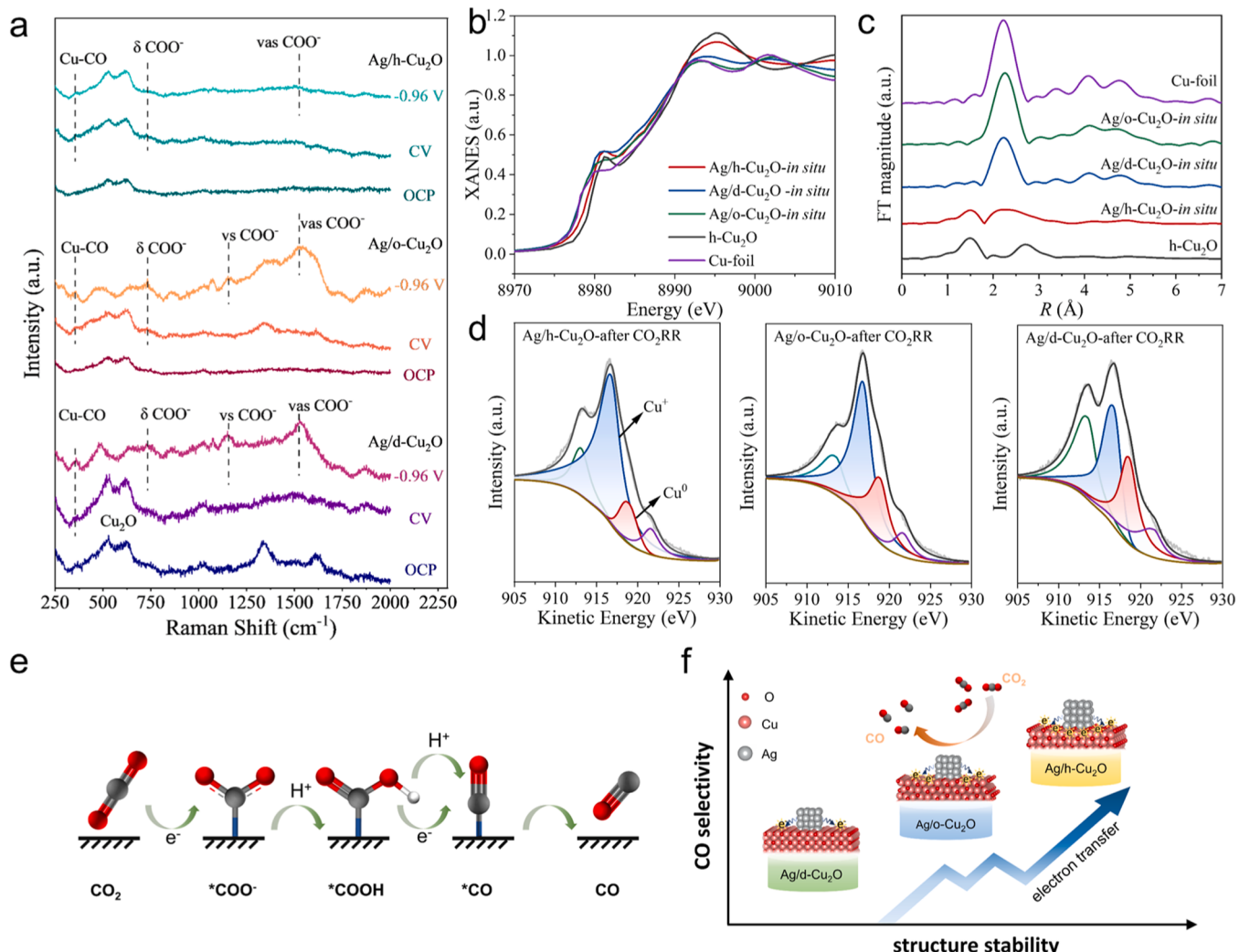


Fig. 5. (a) *In situ* Raman spectra on Ag/h-Cu₂O, Ag/o-Cu₂O and Ag/d-Cu₂O collected at open circuit potential (OCP), activation process (20 CV cycles from 0 to -0.5 V_{RHE}) and the applied potential in CO₂-saturated 0.1 M KHCO₃. (b) Cu K-edge XANES spectra and (c) EXAFS spectra of Ag/h-Cu₂O, Ag/o-Cu₂O and Ag/d-Cu₂O under CO₂RR conditions (-0.96 V vs. RHE in 0.1 M KHCO₃) as well as counterparts. (d) Cu LMM Auger spectra of Ag/h-Cu₂O, Ag/o-Cu₂O and Ag/d-Cu₂O after electrocatalytic CO₂RR. (e) Schematic illustration for reaction path of CO₂RR to CO. (f) Structure-activity relationship between different Ag/Cu₂O systems and CO₂RR.

suggested its structural stability induced by strong component interaction (Fig. S35-S38).

The plausible catalytic reaction mechanisms accompanied by behaviors of catalysts were conjectured. As we know, except for producing formate, CO₂RR generally involves the process of CO₂ → *CO₂ → *COOH → *CO. Whereafter, adsorbed *CO intermediate could transform into gaseous CO or undergo hydrogenation/C-C coupling to form CH₄ and C₂⁺ products. In practice, the reactive selectivity and activity highly depend on the stability of integrated structure and the states of active sites. As proved by DFT calculations and experiment results, the strong electron transfer could stabilize the integrated configuration of Ag/h-Cu₂O and suppressed drastic structural evolution. In contrast, both Ag/o-Cu₂O and Ag/d-Cu₂O underwent severe reduction of Cu⁺ to Cu⁰ and structural collapse due to their weak interfacial interaction (Fig. S39). The stable integral structure of Ag/h-Cu₂O provides a relatively well-organized platform with elaborate active sites for highly selective electrocatalysis rather than unpredictable catalytic matrixes and sites evolved from the unstable Ag/o-Cu₂O and Ag/d-Cu₂O. Meanwhile, the ability to form and stabilize *CO₂ and *COOH intermediates is crucial for an efficient catalyst, which can be assessed by adsorption of surface OH⁻ [47]. The results of LSV measurements demonstrated that

Ag/h-Cu₂O exhibited the highest OH⁻ adsorption peak, suggesting that it had more optimized active sites for generating and stabilizing *CO₂ and *COOH intermediates (Fig. S40). The enhanced CO₂-to-CO reaction energetics and charge transfer kinetics of Ag/h-Cu₂O should allow more electrons to be transferred to CO₂ rather than Cu⁺, thereby further solidifying its self-structure. Thus, the high electrocatalytic activity and selectivity of Ag/h-Cu₂O should be attributed to its relatively stable integrated structure and optimized active sites which originate from rational interfacial interplay.

4. Conclusions

In summary, the study focused on the facet-dependent MSI and its roles in CO₂ electroreduction through the construction of diverse Ag/Cu₂O prototypes. Specific charge redistributed interfaces can be created by electron transfer from Ag to different exposed facets of Cu₂O induced by electric potential difference, which have implication for the stability of the integrated structure and catalytic kinetics. The elaborate heterogeneous interface of Ag/h-Cu₂O could afford optimized active sites with pronounced adsorption capacity for CO₂ molecules and favorable catalytic energetics. Importantly, *in situ* experiments unraveled that Ag/h-

Cu_2O exhibited the strongest MSI in comparison with $\text{Ag}/\text{o}-\text{Cu}_2\text{O}$ and $\text{Ag}/\text{d}-\text{Cu}_2\text{O}$, which suppressed the dramatic structural evolution caused by reduction of Cu^+ under electrochemical condition. Consequently, the FE of CO production reached 93%, along with a partial current density of $6.5 \text{ mA}\cdot\text{cm}^{-2}$ for $\text{Ag}/\text{h}-\text{Cu}_2\text{O}$, surpassing its counterparts. This work provides a new sight into manipulating the MSI to enhance electrocatalysis processes.

CRediT authorship contribution statement

Lidong Wang: Writing – review & editing, Funding acquisition.
Yuheng Wang: Software. **Xiaoxue Xu:** Software. **Zhongfei Xu:** Writing – review & editing, Software. **Juzhe Liu:** Writing – review & editing, Funding acquisition, Data curation. **Zhixiang Cheng:** Investigation. **Jinmeng Li:** Writing – original draft, Visualization, Methodology, Conceptualization. **Hanxia Chen:** Software. **Junpeng Zhu:** Investigation.

Declaration of Competing Interest

The authors declare that they have no known competing financial interests or personal relationships that could have appeared to influence the work reported in this paper.

Data availability

Data will be made available on request.

Acknowledgments

This research was supported by the National Science Fund for Distinguished Young Scholars (No. 52325004), the National Natural Science Foundation of China (No. 22276051, No. 21706061, No. 22176057, No. 21876157, and No. 52302092), Fundamental Research Funds for the Central Universities (No. 2023MS057).

Appendix A. Supporting information

Supplementary data associated with this article can be found in the online version at [doi:10.1016/j.apcatb.2024.124049](https://doi.org/10.1016/j.apcatb.2024.124049).

References

- [1] H.H. Wang, N. Wen, Y. Wang, X. Jiao, Y. Xia, D. Chen, Boosting electrochemical reduction of CO_2 to formate over oxygen vacancy stabilized copper-tin dual single atoms catalysts, *Adv. Funct. Mater.* (2023) 2303473.
- [2] A.R. Woldu, Z.L. Huang, P.X. Zhao, L.S. Hu, D. Astruc, Electrochemical CO_2 reduction (CO_2RR) to multi-carbon products over copper-based catalysts, *Coord. Chem. Rev.* 454 (2022) 214340.
- [3] T.K. Todorova, M.W. Schreiber, M. Fontecave, Mechanistic understanding of CO_2 reduction reaction (CO_2RR) toward multicarbon products by heterogeneous copper-based catalysts, *ACS Catal.* 10 (2020) 1754–1768.
- [4] H. Li, K. Jiang, S.Z. Zou, W.B. Cai, Fundamental aspects in CO_2 electroreduction reaction and solutions from *in situ* vibrational spectroscopies, *Chin. J. Chem. Eng.* 43 (2022) 2772–2791.
- [5] M.Z. Sun, H.H. Wong, T. Wu, Q. Lu, L. Lu, C.H. Chan, B. Chen, A.W. Dougherty, B. Huang, Double-dependence correlations in graphdiyne-supported atomic catalysts to promote CO_2RR toward the generation of C_2 products, *Adv. Energy Mater.* 13 (2023) 2203858.
- [6] Z. Li, R. Wu, L. Zhao, P. Li, X. Wei, J. Wang, J.S. Chen, T. Zhang, Metal-support interactions in designing noble metal-based catalysts for electrochemical CO_2 reduction: recent advances and future perspectives, *Nano Res.* 14 (2021) 3795–3809.
- [7] M. Monai, K. Jenkinson, A.E.M. Melcherts, J.N. Louwen, E.A. Irmak, S.V. Aert, T. Altantzis, C. Vogt, W. v.d. Stam, T. Duchon, B. Šmid, E. Groeneveld, P. Berben, S. Bals, B.M. Weckhuysen, Restructuring of titanium oxide overlayers over nickel nanoparticles during catalysis, *Science* 380 (2023) 644–651.
- [8] J.L. Zhang, W. Sun, L. Ding, Z. Wu, F. Gao, Au nanocrystals@defective amorphous MnO_2 nanosheets core/shell nanostructure with effective CO_2 adsorption and activation toward CO_2 electroreduction to CO, *ACS Sustain. Chem. Eng.* 9 (2021) 5230–5239.
- [9] H.H. Zhai, P. Tan, M. Jiang, M. Zhang, R. Ren, R. Sa, J. Pan, Electronic regulation of Pt single-atom catalysts via local coordination state adjustment for enhanced photocatalytic performance, *ACS Catal.* 13 (2023) 8063–8072.
- [10] M.G. Chu, C.J. Chen, Y.H. Wu, X.P. Yan, S.Q. Jia, R.T. Feng, H.H. Wu, M.Y. He, B. X. Han, Enhanced CO_2 electroreduction to ethylene via strong metal-support interaction, *Green. Energy Environ.* 7 (2022) 792–798.
- [11] X.C. Sun, K. Yuan, J.-H. Zhou, C.-Y. Yuan, H.-C. Liu, Y.-W. Zhang, Au^{3+} species-induced interfacial activation enhances metal-support interactions for boosting electrocatalytic CO_2 reduction to CO, *ACS Catal.* 12 (2022) 923–934.
- [12] H.X. Wang, Y.-K. Tzeng, Y. Ji, Y. Li, J. Li, X. Zheng, A. Yang, Y. Liu, Y. Gong, L. Cai, Y. Li, X. Zhang, W. Chen, B. Liu, H. Lu, N.A. Melosh, Z.-X. Shen, K. Chan, T. Tan, S. Chu, Y. Cui, Synergistic enhancement of electrocatalytic CO_2 reduction to C_2 oxygenates at nitrogen-doped nanodiamonds/Cu interface, *Nat. Nanotechnol.* 15 (2020) 131–137.
- [13] J.R. Yang, W.H. Li, D.S. Wang, Y.D. Li, Electronic metal-support interaction of single-atom catalysts and applications in electrocatalysis, *Adv. Mater.* 32 (2020) 2003300.
- [14] L.C. Liu, X. Gu, Y. Cao, X. Yao, L. Zhang, C. Tang, F. Gao, L. Dong, Crystal-plane effects on the catalytic properties of Au/TiO_2 , *ACS Catal.* 3 (2013) 2768–2775.
- [15] J. Mao, L. Ye, K. Li, X. Zhang, J. Liu, T. Peng, L. Zan, Pt-loading reverses the photocatalytic activity order of anatase TiO_2 {001} and {010} facets for photoreduction of CO_2 to CH_4 , *Appl. Catal. B Environ.* 144 (2014) 855–862.
- [16] Z. Hu, Z. Zou, A. Xie, C. Chen, X. Zhu, Y. Zhang, H. Zhang, H. Zhao, G. Wang, Crystal plane effect of ceria on supported copper catalyst for liquid-phase hydrogenation of unsaturated aldehyde, *J. Colloid Interface Sci.* 596 (2021) 34–43.
- [17] S.B. Liu, X.Z. Wang, H.B. Tao, T.F. Li, Q. Liu, Z.H. Xu, X.Z. Fu, J.L. Luo, Ultrathin 5-fold twinned sub-25 nm silver nanowires enable highly selective electroreduction of CO_2 to CO, *Nano Energy* 45 (2018) 456–462.
- [18] Z. Li, R. Wu, L. Zhao, P.B. Li, X.X. Wei, J.J. Wang, J.S. Chen, T.R. Zhang, Metal-support interactions in designing noble metal-based catalysts for electrochemical CO_2 reduction: Recent advances and future perspectives, *Nano Res.* 14 (2021) 3795–3809.
- [19] H.Q. Luo, B. Li, J.G. Ma, P. Cheng, Surface modification of nano- Cu_2O for controlling CO_2 electrochemical reduction to ethylene and syngas, *Angew. Chem. Int. Ed.* 61 (2022) e202116736.
- [20] K. Wang, M. Lv, T. Si, X. Tang, H. Wang, Y. Chen, T. Zhou, Mechanism analysis of surface structure-regulated Cu_2O in photocatalytic antibacterial process, *J. Hazard. Mater.* 461 (2024) 132479.
- [21] X.T. Ma, Y.G. Zhang, T.T. Fan, D.Y. Wei, Z.Y. Huang, Z.H. Zhang, Z. Zhang, Y. Y. Dong, Q.M. Hong, Z. Chen, X.D. Yi, Facet dopant regulation of Cu_2O boosts electrocatalytic CO_2 reduction to formate, *Adv. Funct. Mater.* 33 (2023) 2213145.
- [22] J. Lin, W. Hao, Y. Shang, X.T. Wang, D.L. Qiu, G.S. Ma, C. Chen, S.Z. Li, L. Guo, Direct experimental observation of facet-dependent SERS of Cu_2O polyhedra, *Small* 14 (2018) 1703274.
- [23] Z.Z. Wu, X.L. Zhang, Z.Z. Niu, F.Y. Gao, P.P. Yang, L.P. Chi, L. Shi, W.S. Wei, R. Liu, Z. Chen, S.J. Hu, X. Zheng, M.R. Gao, Identification of Cu(100)/Cu(111) Interfaces as superior active sites for CO dimerization during CO_2 electroreduction, *J. Am. Chem. Soc.* 144 (2022) 259–269.
- [24] Y. Shang, D. Sun, Y.M. Shao, D.F. Zhang, L. Guo, S.H. Yang, A facile top-down etching to create a Cu_2O jagged polyhedron covered with numerous {110} edges and {111} corners with enhanced photocatalytic activity, *Chem. Eur. J.* 18 (2012) 14261–14266.
- [25] M.L. Zhang, Z.D. Zhang, Z.H. Zhao, H. Huang, D.H. Anjum, D.S. Wang, J.H. He, K. W. Huang, Tunable selectivity for electrochemical CO_2 reduction by bimetallic Cu-Sn catalysts: elucidating the roles of Cu and Sn, *ACS Catal.* 11 (2021) 11103–11108.
- [26] A. Sarmah, P. Hobza, Understanding the non-covalent interaction mediated modulations on the electronic structure of quasi-zero-dimensional graphene nanoflakes, *Phys. Chem. Chem. Phys.* 20 (2018) 18718–18728.
- [27] D.F. Zhang, H. Zhang, L. Guo, K. Zheng, X.-D. Han, Z. Zhang, Delicate control of crystallographic facet-oriented Cu_2O nanocrystals and the correlated adsorption ability, *J. Mater. Chem. I* 19 (2009) 5220–5225.
- [28] B. Qin, Y.B. Zhao, H. Li, L. Qiu, Z. Fan, Facet-dependent performance of Cu_2O nanocrystal for photocatalytic reduction of Cr(VI), *Chin. J. Chem. Eng.* 36 (2015) 1321–1325.
- [29] Y. Deng, C.A. Wan, C. Li, Y.Y. Wang, X.Y. Mu, W. Liu, Y.P. Huang, P.K. Wong, L. Q. Ye, Synergy effect between facet and zero-valent copper for selectivity photocatalytic methane formation from CO_2 , *ACS Catal.* 12 (2022) 4526–4533.
- [30] P. Wang, H. Yang, C. Tang, Y. Wu, Y. Zheng, T. Cheng, K. Davey, X. Huang, S.-Z. Qiao, Boosting electrocatalytic CO_2 -to-ethanol production via asymmetric C-C coupling, *Nat. Commun.* 13 (2022) 3754.
- [31] F.Q. Huang, G. M, J. Liu, J. Lin, X. Wang, L. Guo, High-yield synthesis of hollow octahedral silver nanocages with controllable pack density and their high-performance sers application, *Small* 12 (2016) 5442–5448.
- [32] Y.B. Ma, J. Yu, M. Sun, B. Chen, X. Zhou, C. Ye, Z. Guan, W. Guo, G. Wang, S. Lu, D. Xia, Y. Wang, Z. He, L. Zheng, Q. Yun, L. Wang, J. Zhou, P. Lu, J. Yin, Y. Zhao, Z. Luo, L. Zhai, L. Liao, Z. Zhu, R. Ye, Y. Chen, Y. Lu, S. Xi, B. Huang, C.-S. Lee, Z. Fan, Confined growth of silver-copper janus nanostructures with {100} facets for highly selective tandem electrocatalytic carbon dioxide reduction, *Adv. Mater.* 34 (2022) 2110607.
- [33] L.L. Li, X. Chen, Y. Wu, D. Wang, Q. Peng, G. Zhou, Y. Li, Pd- Cu_2O and Ag- Cu_2O hybrid concave nanomaterials for an effective synergistic catalyst, *Angew. Chem.* 125 (2013) 11255–11259.
- [34] L.H. Tseng, Y.H. Yang, Y.T. Chen, L.C. Hsu, Tailoring copper chemical status and hydrophobicity of biomimetic photocatalytic films for carbon dioxide conversion, *ACS Appl. Mater. Interfaces* 15 (2023) 5038–5048.

- [35] L.Y. Yang, L. Chen, Y.-C. Chen, L. Kang, J. Yu, Y. Wang, C. Lu, T. Mashimo, A. Yoshiasa, C.-H. Lin, Homogeneously alloyed nanoparticles of immiscible Ag-Cu with ultrahigh antibacterial activity, *Colloids Surf. B Biointerfaces* 180 (2019) 466–472.
- [36] H. Deng, Y.B. Yu, F.D. Liu, J.Z. Ma, Y. Zhang, H. He, Nature of Ag species on Ag/ γ -Al₂O₃: a combined experimental and theoretical study, *ACS Catal.* 4 (2014) 2776–2784.
- [37] Q. Wei, Y. Wang, H. Qin, J. Wu, Y. Lu, H. Chi, F. Yang, B. Zhou, H. Yu, J. Liu, Construction of rGO wrapping octahedral Ag-Cu₂O heterostructure for enhanced visible light photocatalytic activity, *Appl. Catal. B Environ.* 227 (2018) 132–144.
- [38] S.J. Li, W. Chen, X. Dong, C. Zhu, A. Chen, Y. Song, G. Li, W. Wei, Y. Sun, Hierarchical micro/nanostructured silver hollow fiber boosts electroreduction of carbon dioxide, *Nat. Commun.* 13 (2022) 3080.
- [39] B.Q. Liu, X. Yao, Z. Zhang, C. Li, J. Zhang, P. Wang, J. Zhao, Y. Guo, J. Sun, C. Zhao, Synthesis of Cu₂O nanostructures with tunable crystal facets for electrochemical CO₂ reduction to alcohols, *ACS Appl. Mater. Interfaces* 13 (2021) 39165–39177.
- [40] A. Herzog, A. Bergmann, H.S. Jeon, J. Timoshenko, S. Kühl, C. Rettenmaier, M. L. Luna, F.T. Haase, B.R. Cuenya, *Operando* investigation of Ag-decorated Cu₂O nanocube catalysts with enhanced CO₂ electroreduction toward liquid products, *Angew. Chem. Int. Ed.* 60 (2021) 7426–7435.
- [41] Z.P. Ma, T. Wan, D. Zhang, J.A. Yuwono, C. Tsounis, J. Jiang, Y.-H. Chou, X. Lu, P. V. Kumar, Y.H. Ng, D. Chu, C.Y. Toe, Z. Han, R. Amal, Atomically dispersed Cu catalysts on sulfide- derived defective Ag nanowires for electrochemical CO₂ reduction, *ACS Nano* 17 (2023) 2387–2398.
- [42] W.Y. Shan, R. Liu, H. Zhao, Z. He, Y. Lai, S. Li, G. He, J. Liu, In situ surface-enhanced Raman spectroscopic evidence on the origin of selectivity in CO₂ electrocatalytic reduction, *ACS Nano* 14 (2020) 11363–11372.
- [43] Y.X. Zhou, Y.B. Yao, R. Zhao, X.X. Wang, Z.Z. Fu, D.W. Wang, H.Z. Wang, L. Zhao, W. Ni, Z.Y. Yang, Y.M. Yan, Stabilization of Cu⁺ via strong electronic interaction for selective and stable CO₂ electroreduction, *Angew. Chem. Int. Ed.* 61 (2022) e202205832.
- [44] H.J. Shi, L.L. Luo, C.C. Li, Y. Li, T.T. Zhang, Z.L. Liu, J.L. Cui, L. Gu, L. Zhang, Y. J. Hu, H.H. Li, C.Z. Li, Stabilizing Cu⁺ species in Cu₂O/CuO catalyst via carbonIntermediate confinement for selective CO₂RR, *Adv. Funct. Mater.* (2023) 2310913.
- [45] H.F. Li, T.F. Liu, P.F. Wei, L. Lin, D.F. Gao, G.X. Wang, X.H. Bao, High-Rate CO₂ Electroreduction to C₂⁺ Products over a Copper-Copper Iodide Catalyst, *Angew. Chem. Int. Ed.* 60 (2021) 14329–14333.
- [46] P.P. Yang, X.L. Zhang, F.Y. Gao, Y.R. Zheng, Z.Z. Niu, X.X. Yu, R. Liu, Z.Z. Wu, S. Qin, L.P. Chi, Y. Duan, T. Ma, X.S. Zheng, J.F. Zhu, H.J. Wang, M.R. Gao, S. H. Yu, Protecting copper oxidation state via intermediate confinement for selective CO₂ electroreduction to C₂⁺ fuels, *J. Am. Chem. Soc.* 142 (2020) 6400–6408.
- [47] H.Q. Fu, J. Liu, N.M. Bedford, Y. Wang, J.W. Sun, Y. Zou, M. Dong, J. Wright, H. Diao, P. Liu, H.G. Yang, H. Zhao, Synergistic Cr₂O₃@Ag heterostructure enhanced electrocatalytic CO₂ reduction to CO, *Adv. Mater.* 34 (2022) 2202854.